

ADA077115

UNCLASSIFIED

SECURITY CLASSIFICATION OF THIS PAGE (When Data Entered)

REPORT DOCUMENTATION PAGE		READ INSTRUCTIONS BEFORE COMPLETING FORM
1. REPORT NUMBER 11.1 11.1	2. GOVT ACCESSION NO.	3. RECIPIENT'S CATALOG NUMBER
4. TITLE (and Subtitle) NAVIER-STOKES SOLUTIONS FOR SPIN-UP FROM REST IN A CYLINDRICAL CONTAINER		5. TYPE OF REPORT & PERIOD COVERED 9 Final
6. AUTHOR(s) C. W. Kitchens, Jr.		7. PERFORMING ORG. REPORT NUMBER
8. CONTRACT OR GRANT NUMBER(s)		9. PROGRAM ELEMENT, PROJECT, TASK AREA & WORK UNIT NUMBERS RD6E 1L161102AH43 1L162618AH80
10. PERFORMING ORGANIZATION NAME AND ADDRESS U.S. Army Ballistic Research Laboratory ATTN: DRDAR-BLT Aberdeen Proving Ground, MD 21005		11. REPORT DATE SEPTEMBER 79 NUMBER OF PAGES 55
12. CONTROLLING OFFICE NAME AND ADDRESS U.S. Army Armament Research and Development Command U.S. Army Ballistic Research Laboratory (ATTN: DRDAR-BL) Aberdeen Proving Ground, MD 21005		13. SECURITY CLASS. (of this report) UNCLASSIFIED
14. MONITORING AGENCY NAME & ADDRESS (if different from Controlling Office)		15. DECLASSIFICATION/DOWNGRADING SCHEDULE
16. DISTRIBUTION STATEMENT (of this Report) Approved for public release; distribution unlimited.		
17. DISTRIBUTION STATEMENT (of the abstract entered in Block 20, if different from Report)		
18. SUPPLEMENTARY NOTES		
19. KEY WORDS (Continue on reverse side if necessary and identify by block number) Spin-up Compatibility condition Liquid-filled shell Wedemeyer model Ekman layer Inertial oscillation Navier-Stokes Rotating fluids Numerical methods		
20. ABSTRACT (Continue on reverse side if necessary and identify by block number) (mba) An accurate and efficient predictor-corrector multiple-iteration scheme is adapted and used for the first time to solve the unsteady Navier-Stokes equations. Numerical solutions for Reynolds numbers up to 50,000 are obtained for the transient spin-up flow in a cylindrical container. The grid point distribution is optimized using coordinate transformations to simultaneously resolve details of both the interior and endwall/sidewall boundary layer flows formed during spin-up. Calculations for five test problems show consistency with previous computations and/or experimental measurements. Transient phenomena		

(Continued)

DD FORM 1 JAN 73 1473

EDITION OF 1 NOV 65 IS OBSOLETE

UNCLASSIFIED

SECURITY CLASSIFICATION OF THIS PAGE (When Data Entered)

393 471

JCB

UNCLASSIFIED

SECURITY CLASSIFICATION OF THIS PAGE(When Data Entered)

(Item 20 continued)

occurring at early time near the sidewall, including inertial oscillations and counter-rotating meridional flow, are reported and discussed. Computational experiments have been used to quantify the mass flow in the endwall boundary layers and investigate the compatibility condition used in Wedemeyer's spin-up model.

A

Accession For	
NTIS GRA&I	<input checked="" type="checkbox"/>
DGC TAB	
Unannounced Justification	
By _____	
Distribution _____	
Availability or special	
Dist.	

UNCLASSIFIED

SECURITY CLASSIFICATION OF THIS PAGE(When Data Entered)

TABLE OF CONTENTS

	Page
LIST OF ILLUSTRATIONS	5
I. INTRODUCTION	7
II. GOVERNING EQUATIONS AND BOUNDARY CONDITIONS	8
III. NUMERICAL PROCEDURE	10
IV. STABILITY PROPERTIES OF NUMERICAL PROCEDURE	18
V. COMPARISON WITH PREVIOUS WORK	18
VI. TRANSIENT PHENOMENA AT EARLY TIME	25
VII. EKMAN LAYER MASS FLOW AND COMPATIBILITY CONDITION DURING SPIN-UP	30
VIII. CONCLUSIONS	39
APPENDIX A - TRANSFORMED EQUATIONS AND BOUNDARY CONDITIONS	41
APPENDIX B - FINITE-DIFFERENCE EQUATIONS	43
LIST OF SYMBOLS	47
DISTRIBUTION LIST	49

LIST OF ILLUSTRATIONS

Figure	Page
1. Geometry for spin-up calculations	11
2. Typical grid point distribution in physical plane shown for coarse 11 x 21 grid with $\alpha = 2$ and $d = e = 0.05$	12
3. Grid point stencil with differences centered at (i + 1, j, k)	15
4. Inertial oscillations during spin-up from a previous state of rigid-body rotation	19
5. Comparison of inertial oscillations during spin-up from rest and from a previous state of rigid-body rotation	21
6. Rotational volume flow rate for spin-up from rest	22
7. Azimuthal velocity profiles at cylinder mid-plane for $\alpha = 1.515$, $Re = 3076$	23
8. Azimuthal velocity profiles at cylinder mid-plane for $\alpha = 1$, $Re = 9741.6$	24
9a. Instantaneous streamlines in meridional plane for $\alpha = 1$, $Re = 9741.6$, $\Delta\psi = 0.0004$; $t = 3$; $\psi_{min} = 0$, $\psi_{max} = 0.00322$	26
9b. Streamlines for $t = 6$; $\psi_{min} = -0.00003$, $\psi_{max} = 0.00350$. Closed contour along sidewall indicates reversed flow region	27
9c. Streamlines for $t = 20$; $\psi_{min} = -0.00003$, $\psi_{max} = 0.00294$	28
9d. Streamlines for $t = 24$; $\psi_{min} = 0$, $\psi_{max} = 0.00284$	29
10. Instantaneous streamlines for $\alpha = 1$, $Re = 50,000$ $t = 15$, with $\Delta\psi = 0.0004$; $\psi_{min} = -0.00013$, $\psi_{max} = 0.00177$	31
11. Ekman layer compatibility conditions	33
12. Radial velocity profiles in Ekman layer at $r = 0.76$ for $\alpha = 1$, $Re = 9741.6$ and $t = 8.3$	34

LIST OF ILLUSTRATIONS

Figure		Page
13.	Ekman layer radial mass flow predicted for $\alpha = 2$, Re = 9741.6 using Richardson extrapolation	36
14.	Comparison of compatibility conditions with band representing numerical data for $1 \leq \alpha \leq 4.4$ and $405 \leq \text{Re} \leq 50,000$	38

1. INTRODUCTION

The objective of this work is to develop an accurate and efficient numerical procedure for solving the unsteady Navier-Stokes equations to describe transient spin-up flow occurring in a cylindrical container when it is suddenly rotated about its longitudinal axis. Knowledge of this internal flow is needed to design gun-launched projectiles which carry smoke/incendiary agents or chemical payloads. Liquid payloads enhance spin decay of projectiles^{1,2} and their presence can produce flight dynamic instabilities as a result of resonance between the projectile nutational motion and inertial oscillations in the rotating liquid³. From a computational viewpoint this problem is instructive because it is an example of a class of internal flow problems for which computational experiments can uncover details of the flow that cannot be easily visualized or measured experimentally.

The results presented here demonstrate that a predictor-corrector multiple-iteration (PCMI) technique developed by Rubin and Lin⁴ for solving steady three-dimensional boundary region problems can be successfully adapted to solve the unsteady Navier-Stokes equations. In the present approach this method is combined with the Gauss-Seidel procedure⁵ and grid stretching transformations to produce an accurate and efficient numerical procedure for describing the spin-up process. Calculations with the PCMI method have been performed for spin-up from rest and spin-up from an initial state of solid-body rotation; in both types of problems inertial oscillations have developed in the rotating liquids. Numerical results have been obtained for a range of cylinder aspect ratios, α , from 0.3 to 4.4 and a range of Reynolds numbers from 215 to 50,000. Calculations performed for five test problems are consistent

¹E. H. Wedemeyer, "The Unsteady Flow Within a Spinning Cylinder," *J. Fluid Mech.*, Vol. 20, Pt. 3, 1964, pp. 383-399; also see BRL Report 1562, Aberdeen Proving Ground, MD, AD 431846, Oct. 1963.

²C. W. Kitchens, Jr., N. Gerber and R. Sedney, "Spin Decay of Liquid-Filled Projectiles," *J. Spacecraft and Rockets*, Vol. 15, No. 6, Nov-Dec 1978, pp. 348-354.

³K. Stewartson, "On the Stability of a Spinning Top Containing Liquid," *J. Fluid Mech.*, Vol. 5, Pt. 4, Sept. 1959, pp. 577-592.

⁴S. G. Rubin and T. C. Lin, "A Numerical Method for Three-Dimensional Viscous Flow: Application to the Hypersonic Leading Edge," *J. Comp. Phys.*, Vol. 9, 1972, pp. 339-364.

⁵M. G. Salvadori and M. L. Baron, *Numerical Methods in Engineering*, Prentice-Hall, Inc., Englewood Cliffs, N. J., 1961.

with previous computations^{6,7,8} and experimental measurements^{6,9}. Numerical results have also been used to quantify the flow in the Ekman (or endwall) boundary layers during spin-up and thus develop an appropriate "compatibility condition" for use in Wedemeyer's model¹ for spin-up from rest. Although the results are not discussed here, the PCMI procedure has been used to obtain spin-up flow in the annulus between finite-length, concentric cylinders. Neitzel¹⁰ also used the PCMI computer program to study the onset and temporal development of fluid dynamic instabilities during spin down in a cylinder.

II. GOVERNING EQUATIONS AND BOUNDARY CONDITIONS

The calculations employ a finite-difference analog of the unsteady axisymmetric Navier-Stokes equations formulated in cylindrical coordinates (r, θ, z) . The equations are expressed in terms of stream function, ψ , vorticity, ζ , and circulation, γ , instead of velocity and pressure in order to simplify the numerical procedure. In dimensionless variables the governing equations are

$$\nabla^2 \psi - \psi/r = r\zeta, \quad (1)$$

$$\zeta_t + u\zeta_r + w\zeta_z - u\zeta/r - 2\gamma\gamma_z/r^3 = (1/Re)[\nabla^2 \zeta + \zeta_r/r - \zeta/r^2], \quad (2)$$

$$\gamma_t + u\gamma_r + w\gamma_z = (1/Re)[\nabla^2 \gamma - \gamma/r]; \quad (3)$$

where the subscripts denote partial differentiation and

$$Re = \Omega a^2/\nu, \quad (4)$$

⁶A. Nemi-Varnas, W. W. Fowles, S. Piacsek and S. M. Lee, "Numerical Solutions and Laser Doppler Measurements of Spin-Up," *J. Fluid Mech.*, Vol. 85, Pt. 4, 1978, pp. 609-639.

⁷W. R. Briley, "Time Dependent Rotating Flow in a Cylindrical Container," PhD Dissertation, The University of Texas at Austin, 1968, University Microfilms, Inc., 69-6121.

⁸W. R. Briley and H. A. Walle, "A Numerical Study of Time-Dependent Rotating Flow in a Cylindrical Container at Low and Moderate Reynolds Numbers," *Proc. 2nd Intl. Conf. on Num. Meth.Fld. Dyn., Lecture Notes in Physics*, Vol. 8, Springer-Verlag, 1970, pp. 377-384.

⁹W. B. Watkins and R. G. Hussey, "Spin-Up From Rest in a Cylinder," *Phys. of Fluids*, Vol. 20, No. 10, Pt. 1, 1977, pp. 1598-1604.

¹⁰G. P. Neitzel, Jr., "Centrifugal Instability of Decelerating Swirl Flow within Finite and Infinite Circular Cylinders," PhD Dissertation, The John Hopkins University, Baltimore, MD. 1979.

$$\nabla^2 = \partial^2/\partial r^2 + \partial^2/\partial z^2, \quad (5)$$

$$\gamma = r v, \quad (6)$$

$$\zeta = u_z - w_r, \quad (7)$$

with the axisymmetric stream function defined so that

$$u = \psi_z/r \text{ and } w = -\psi_r/r. \quad (8)$$

The Ekman number based on half-height is related to Re by

$$Ek = \nu/(\Omega a^2) = 1/(\Omega Re).$$

The stream function-vorticity-circulation formulation yields an elliptic PDE, Equation (1), and two parabolic PDEs, Equations (2) and (3), which are coupled. The boundary conditions impose additional coupling between ψ and ζ .

The nondimensional variables used here are formed by

$$\begin{aligned} r &= R/a, \quad z = Z/a, \quad t = \Omega T, \\ u &= U/(\Omega a), \quad v = V/(\Omega a), \quad w = W/(\Omega a), \\ \psi &= \psi/(\Omega a^3), \quad \gamma = \Gamma/(\Omega a^2), \quad \zeta = Z/\Omega. \end{aligned} \quad (9)$$

The initial conditions for spin-up are

$$\psi = \zeta = 0, \quad \gamma = \Omega_i r^2/\Omega \text{ for } t \leq 0, \quad (10)$$

where Ω_i is the initial cylinder rotation rate. Computational efficiency and resolution are improved by employing a symmetry boundary condition at the cylinder mid-plane, $z = a$. This effectively halves the number of grid points required. The boundary conditions for $t \geq 0$ are

$$\psi(t, 0, z) = \gamma(t, 0, z) = \zeta(t, 0, z) = 0, \quad (11a)$$

$$\psi(t, 1, z) = 0, \quad \gamma(t, 1, z) = 1, \quad \zeta(t, 1, z) = \psi_{rr}(t, 1, z), \quad (11b)$$

$$\psi(t, r, 0) = 0, \quad \gamma(t, r, 0) = r^2, \quad \zeta(t, r, 0) = \psi_{zz}(t, r, 0)/r, \quad (11c)$$

$$\psi(t, r, a) = \zeta(t, r, a) = 0, \quad \gamma_z(t, r, a) = 0. \quad (11d)$$

The boundary conditions for vorticity along the sidewall and endwall, Equations (11b) and (11c), are derived from Equations (7) and (8) by imposing the no-slip conditions for velocity. Figure 1 illustrates the coordinate system and boundaries used in the numerical calculations for spin-up.

During the spin-up process there are viscous regions near the sidewall and endwalls which become very thin as Re becomes larger than 1000 or so, necessitating a fine grid to resolve the boundary-layer type phenomena along these walls. Analytical coordinate transformations are used to optimize the grid point distribution and transform a nonuniform grid in the physical plane into an equally-spaced grid in the computational plane. Transformations based on the work of Roberts¹¹,

$$\bar{b} = \ln [(\bar{b} + r)/(\bar{b} - r)] / \ln [(\bar{b} + 1)/(\bar{b} - 1)], \quad (12a)$$

$$\bar{c} = 1 + \ln [(\bar{c} + z/a - 1)/(\bar{c} - z/a + 1)] / \ln [(\bar{c} + 1)/(\bar{c} - 1)], \quad (12b)$$

with $\bar{b} = (1 - d)^{-1/2}$ and $\bar{c} = (1 - e)^{-1/2}$ are selected. These transformations are particularly suited for problems where thin viscous regions lie along one boundary in each of the coordinate directions. Values of d and e ($0 < d < 1$, $0 < e < 1$) are specified to group a large fraction of the grid points (typically 1/2 or so) into the sidewall and endwall viscous regions where large velocity gradients are present; as d and $e \rightarrow 0$ the grid point spacing becomes finer near the sidewall and endwall, respectively. Figure 2 shows a typical nonuniform grid point distribution in the physical plane produced with these transformations, see Equation (12), using equally-spaced grid points in the computational plane. The complete set of transformed equations and boundary conditions are given in Appendix A.

III. NUMERICAL PROCEDURE

Many methods have been used by previous investigators to solve the stream function-vorticity form of the Navier-Stokes equations. Perhaps the most popular technique is to combine the alternating-direction implicit (ADI) method¹² for the ζ and γ -equations with either an ADI or

¹¹G. O. Roberts, "Computational Meshes for Boundary-Layer Problems," *Proc. 2nd Intl. Conf. on Num. Meth.Fld. Dyn., Lecture Notes in Physics*, Vol. 8, Springer Verlag, 1970, pp. 171-177.

¹²D. W. Peaceman and H. H. Rachford, Jr., "The Numerical Solution of Parabolic and Elliptic Differential Equations," *J. SIAM*, Vol. 3, No. 1, 1955, pp. 28-41.

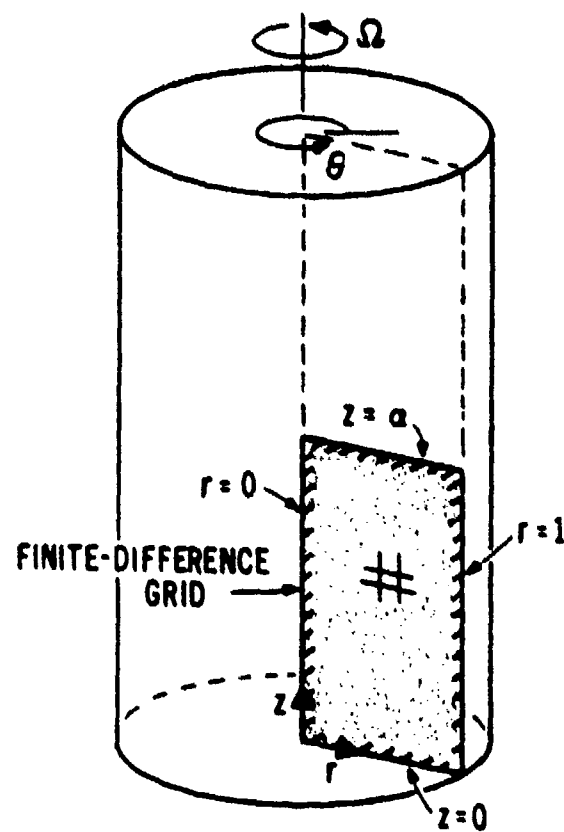


Figure 1. Geometry for spin-up calculations.

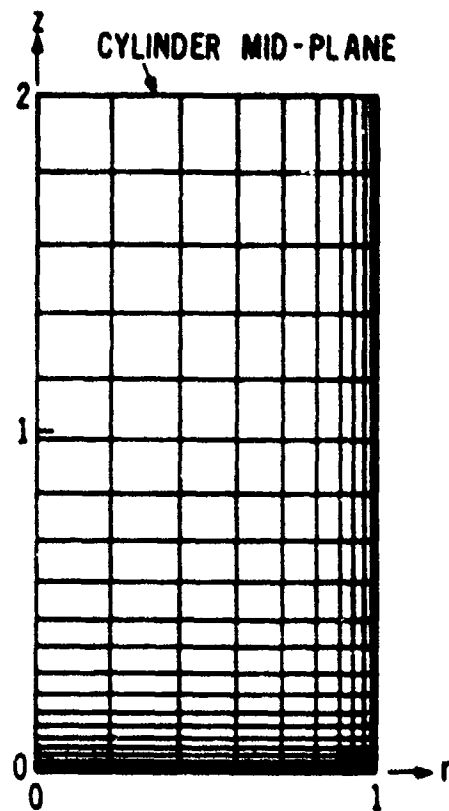


Figure 2. Typical grid point distribution in physical plane shown for coarse 11×21 grid with $\alpha = 2$ and $d = c = 0.05$.

successive over-relaxation (SOR) method¹³ for the ψ -equation. This report describes an efficient alternative procedure for solving the ζ and ψ -equations, namely, the semi-implicit PCMI method. To the best of the author's knowledge this is the first time this method has been used to solve the Navier-Stokes equations. It represents a compromise in approach between the implicit ADI scheme and explicit schemes used by other authors. In the present application the ψ -equation is solved by the Gauss-Seidel method⁵; the SOR method was used for test calculations, but it did not speed up the overall procedure.

In the PCMI method the solution is advanced to a new time level in a single time step Δt as opposed to the two half-time steps required in one cycle of the ADI method. It is implicit in the radial direction; the solution requires only the inversion of a tridiagonal matrix for each row in the computational grid. The ADI procedure, on the other hand, requires that a tridiagonal matrix be solved for each row in the first half-time step, and then for each column in the second half-time step, leading to a longer computation time per full time step.

A symmetry boundary condition, such as $v_z = 0$ along the cylinder mid-plane, is easy to implement in this method since all flow gradients in the z -direction are approximated by prediction and subsequent correction in this time-iteration technique. This approach eliminates the cross coupling of grid points, thus reducing the size of the inversion matrices and decreasing the computer time required. The iteration procedure allows the boundary vorticity to converge and also allows the nonlinear terms to be approximated and then corrected, giving a more accurate simulation of the nonlinear coupling between equations.

Central difference formulae are used for all spatial derivatives at interior points, avoiding false-diffusion effects introduced by upwind difference schemes. Temporal derivatives are approximated by second-order accurate one-sided difference formulae involving three time levels. The following finite-difference representations are used for the ζ -equation:

$$\zeta_\theta = (1/2\Delta\theta) \left[\zeta_{i+1, j+1, k}^{m+1} - \zeta_{i+1, j-1, k}^{m+1} \right], \quad (13a)$$

$$\zeta_{\theta\theta} = (1/\Delta\theta^2) \left[\zeta_{i+1, j+1, k}^{m+1} - 2\zeta_{i+1, j, k}^{m+1} + \zeta_{i+1, j-1, k}^{m+1} \right] \quad (13b)$$

$$\zeta_t = (1/2\Delta t) \left[3\zeta_{i+1, j, k}^{m+1} - 4\zeta_{i, j, k} + \zeta_{i-1, j, k} \right], \quad (13c)$$

¹³D. Young, "Iterative Methods for Solving Partial Difference Equations of Elliptic Type," Trans. Amer. Math. Soc., Vol. 76, 1954, pp. 92-111.

$$\zeta_n = (1/2\Delta n) \left[\zeta_{i+1,j,k+1}^{m+1} - \zeta_{i+1,j,k-1}^m \right], \quad (13d)$$

$$\zeta_{nn} = (1/\Delta n^2) \left[\zeta_{i+1,j,k+1}^{m+1} - 2\zeta_{i+1,j,k}^{m+1} + \zeta_{i+1,j,k-1}^m \right], \quad (13e)$$

$$v_B = (1/2\Delta\delta) \left[v_{i+1,j+1,k}^m - v_{i+1,j-1,k}^m \right], \quad (13f)$$

$$v_n = (1/2\Delta n) \left[v_{i+1,j,k+1}^m - v_{i+1,j,k-1}^m \right], \quad (13g)$$

$$\zeta = \zeta_{i,j,k}^{m+1}, \quad (13h)$$

$$vv_n = (v_{i+1,j,k}^m / 2\Delta n) (v_{i+1,j,k+1}^m - v_{i+1,j,k-1}^m); \quad (13i)$$

where superscript m denotes the time-iteration number. The expressions for the v -equation are identical in form to Equations (13). The finite-difference representations for the v -equation are:

$$v_B = (1/2\Delta\delta) \left[v_{i+1,j+1,k}^{n+1} - v_{i+1,j-1,k}^{n+1} \right], \quad (14a)$$

$$v_{BB} = (1/\Delta\delta^2) \left[v_{i+1,j+1,k}^{n+1} - 2v_{i+1,j,k}^{n+1} + v_{i+1,j-1,k}^{n+1} \right], \quad (14b)$$

$$v_n = (1/2\Delta n) \left[v_{i+1,j,k+1}^{n+1} - v_{i+1,j,k-1}^{n+1} \right], \quad (14c)$$

$$v_{nn} = (1/\Delta n^2) \left[v_{i+1,j,k+1}^{n+1} - 2v_{i+1,j,k}^{n+1} + v_{i+1,j,k-1}^{n+1} \right]; \quad (14d)$$

where superscript n denotes the v -iteration number. Figure 3 shows a finite-difference stencil for this scheme with all derivatives evaluated at $(i+1,j,k)$. The above finite-difference approximations are compact, involving only one time level. This leads to programming simplifications and shorter run times. The complete set of finite-difference equations is given in Appendix B. These finite-difference expressions insure truncation errors for interior points of $O(\Delta t^2, \Delta\delta^2, \Delta n^2)$. The overall

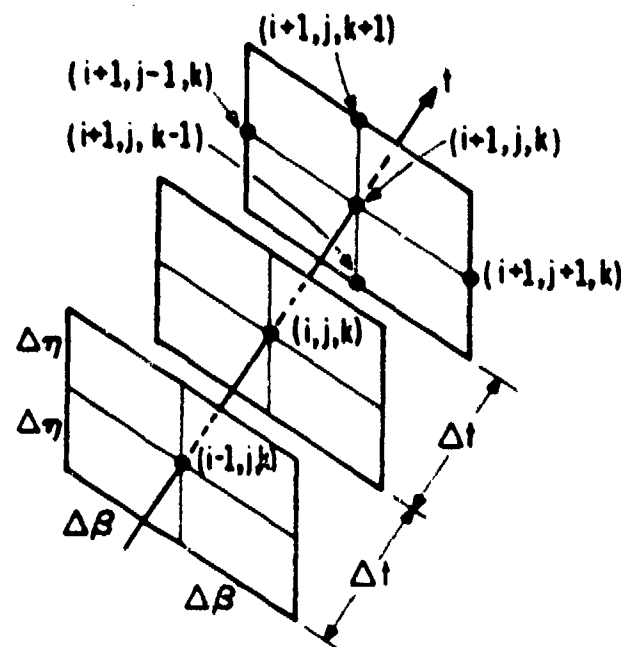


Figure 3. Grid point stencil with differences centered at $(i + 1, j, k)$.

accuracy of the method depends on the treatment of the boundary conditions and this will be discussed later.

The numerical procedure is easy to implement. For the predictor step, or first iteration of each time-iterative cycle, terms in the difference equations with superscript 0 are approximated by a Taylor series to $O(\Delta t^3)$:

$$F_{i+1,j,k}^0 = 3F_{i,j,k}^0 - 3F_{i-1,j,k}^0 + F_{i-2,j,k}^0 + O(\Delta t^3). \quad (15)$$

During the first two time steps extrapolations of $O(\Delta t)$ and $O(\Delta t^2)$ are used, respectively. The use of Equation (15) reduces the number of iterations required to achieve accuracy and stability; these advantages must be weighed against possible storage problems caused by the additional planes of data needed for the extrapolation. The influence of the extrapolation procedure on stability and iteration convergence has been discussed by Rubin and Lin⁴.

After extrapolating guesses for ζ^0 , γ^0 , and ψ^0 at time $(i+1)$, the wall vorticity is determined using the ψ^0 -values and Equations (11b) and (11c). The manner in which this is carried out deserves special comment, since it can often have a strong influence on iteration convergence. In the present calculations we adopt a first-order form for the wall vorticity boundary conditions, expressed in transformed coordinates as

$$\zeta_{\theta=1}^{m+1} = 2(\theta_r)^2 \psi_{w+1}^m / (\Delta \theta^2) + O(\Delta \theta), \quad (16a)$$

$$\zeta_{\eta=0}^{m+1} = 2(\eta_z)^2 \psi_{w+1}^m / (r \Delta \eta^2) + O(\Delta \eta); \quad (16b)$$

where subscript $w+1$ represents the grid point adjacent to each respective wall point. This first-order form is used since it is known to have the least adverse effect on iteration convergence and it often gives results essentially identical to higher-order accurate expressions¹⁴. The numerical procedure used here appears to be fully compatible with second-order accurate expressions for wall vorticity, based on the results of test calculations for $\alpha = 1$, $Re = 1000$. The boundary values for γ along the midplane are determined from the one-sided difference expression

¹⁴C. W. Kitchens, Jr., "Separation and Reattachment Near Square Protuberances in Low Reynolds Number Couette Flow," BRL Report 1695, Aberdeen Proving Ground, MD, AD 773663, Jan. 1974.

$$(\gamma^{m+1})_{n=1} = (4\gamma_{M-1}^m - \gamma_{M-2}^m)/3 + O(\Delta n^2); \quad (17)$$

where M-1 and M-2 represent the first and second points, respectively, adjacent to $n=1$.

With all boundary values now approximated, the difference equations for γ^{m+1} and ζ^{m+1} are solved with the PCMI method using the m-iterate values to form the coefficients of the nonlinear terms. The calculations start along the row of points, M-1, adjacent to the midplane and work downward toward the endwall. The derivatives in the β -direction are treated implicitly, thus requiring the solution of a tridiagonal system of equations along each successive row. The (m+1)-iterate values at (i+1,j,k+1) are used to approximate derivatives in the n -direction at (i+1,j,k) as soon as they become available; see Equations (13d) and (13e).

At the end of each iteration cycle for ζ and γ , the difference form of the stream function equation is solved iteratively by the Gauss-Seidel technique. The solution is obtained by starting at the interior grid point adjacent to $\beta=n=0$ and sweeping first in β and then n , making use of updated values as soon as they become available; see Equations (14). Convergence is assumed when

$$\text{Max}_{j,k} |\gamma^{n+1} - \gamma^n| < \epsilon_1. \quad (18a)$$

This is typically achieved in 2-3 iterations with $\epsilon_1 = 1 \times 10^{-7}$. The converged values for γ are now used to update the boundary values for ζ and repeat the iteration process for γ and ζ . The iteration process is assumed to converge when both

$$\text{Max}_{j,k} |\gamma^{m+1} - \gamma^m| < \epsilon_2, \quad (18b)$$

$$\text{Max}_{j,k} |\zeta^{m+1} - \zeta^m| < \epsilon_3. \quad (18c)$$

It typically requires 2-3 iterations to satisfy Equations (18b, c) with $\epsilon_2 = \epsilon_3 = 1 \times 10^{-4}$; at very early time 5-10 iterations are generally needed due to the severe flow unsteadiness caused by the impulsive start and the subsequent inaccuracy of the extrapolated guesses.

IV. STABILITY PROPERTIES OF NUMERICAL PROCEDURE

Rubin and Lin⁴ have analyzed the interior point stability of the PCMI method for a model linear equation. Their analysis shows that the method is conditionally stable and that with one or more iterations the stability criterion is independent of Re. On the basis of their results the appropriate stability criterion for our calculations is

$$\Delta t \leq \text{Min}_{j,k} [\Delta n / |n_{zz} / \text{Re} + \beta_r n_z v_\theta / r|]. \quad (19)$$

The term in the denominator containing Re results from the coordinate transformation for z; this term vanishes if an equally-spaced grid is used in the z-direction. Equation (19) must be applied cautiously since the governing equations are actually non-linear and the boundary condition treatment has not been included in the analysis.

Numerical tests were conducted to assess the effect of violating the above stability criterion. These tests were conducted for $\alpha = 1$ with $\text{Re} = 1000, 9742$ and $50,000$, using three combinations of grid sizes for each Re and several different values of the transformation parameters d and e. The results show that numerical stability is always achieved when Equation (19) is satisfied. In some cases the PCMI calculations remain stable with Δt as large as 150% of the maximum allowable value. In general, the calculations show that satisfying Equation (19) is sufficient, but not necessary, for numerical stability. Equation (19) was satisfied at each time step in the illustrative examples to be discussed next.

V. COMPARISON WITH PREVIOUS WORK

The present method has been used to treat the problems of spin-up from rest and spin-up from an initial state of solid-body rotation. We compare our results with those of Warn-Varnas et al.⁶ for the latter problem. They used an ADI technique coupled with a scheme developed by Williams¹⁵ to solve the velocity-pressure form of the Navier-Stokes equations. In their calculations they differenced the governing equations directly on a stretched grid instead of transforming to new coordinates as is done here. Their computations were verified by measurements taken with a laser doppler velocimeter (LDV) system.

Figure 4 shows a comparison of the present calculations with results from Reference 6 (their Figure 13b). The comparisons are expressed in terms of their quantity called "zonal velocity" (ordinate in Figure 4)

¹⁵G.P. Williams, "Numerical Integration of the Three-Dimensional Navier-Stokes Equations for Incompressible Flow," J. Fluid Mech., Vol. 37, 1969, pp. 727-760.

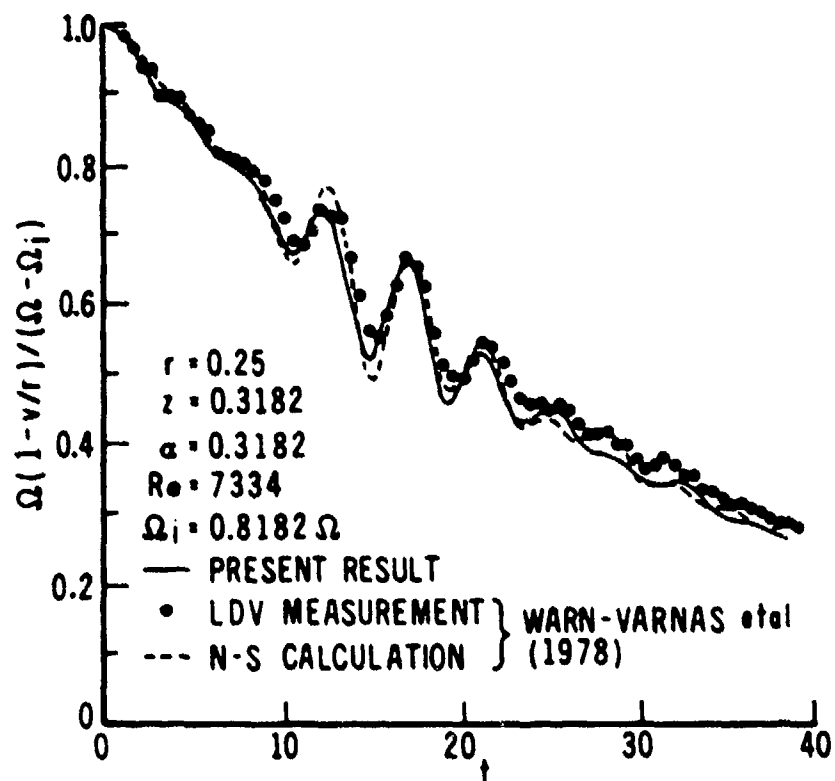


Figure 4. Inertial oscillations during spin-up from a previous state of rigid-body rotation.

which is a scaled non-dimensional angular velocity. The results are shown at $r = 0.25$ on the cylinder symmetry plane for a case with $a = 0.3182$, $Re = 7334$ and $\Omega_i = 0.8182\Omega$. The inertial oscillations excited by the sudden increase in cylinder rotation rate are clearly predicted in both computations and are in fairly good agreement with experimental measurements. Both of these numerical results appear to be within the experimental uncertainty associated with these data, according to the error analysis presented in Reference 6. Comparisons for several other positions in the cylinder (not shown here) give similar agreement for both the decay of the zonal velocity and the amplitudes and phases of the inertial oscillations. The computation time and number of grid points used to obtain the numerical results in Reference 6 are not stated. The PCMI method required 51.5s of CPU time on a CDC 7600 computer using a stretched ($d = 0.3$, $e = 0.1$) 41×21 (r - z) grid with 600 time steps ($\Delta t = 0.063$). Approximately 2-3 iterations were required per time step.

The problem of spin-up from rest has been emphasized in the present work because of its application to liquid-filled projectiles. This problem is, by its nature, nonlinear; the previous problem can be linearized for small $\Omega - \Omega_i$. Figure 5 compares results for zonal velocity for spin-up from rest with those for spin-up from a previous state of rigid-body rotation. The comparison is made at $r = 0.90$ for two values of z , illustrating the axial structure present in these oscillations. For $\Omega_i = 0$, results for both values of z indicate that the frequency of the dominant inertial mode increases with time at the early times shown in Figure 5; the amplitude of these oscillations damps rapidly and cannot be detected for $t > 40$.

Comparisons have been made with computations of Briley⁷ and Briley and Walls⁸ for spin-up from rest. They studied this problem for low Re using the ADI technique to solve the stream function-vorticity form of the Navier-Stokes equations. Figure 6 compares values of rotational volume flow rate,

$$Q = (1/a) \int_0^1 \int_0^{2a} v \, dzdr, \quad (20)$$

for two cases. The quantity Q can be used to obtain a measure of the spin-up time. Briley and Walls used a uniform grid that became restrictive at moderate Re due to the small thickness of the endwall boundary layers; they obtained results for Re as large as 1167. Our calculations appear to be in good agreement with all of their results for spin-up. Neitzel's comparisons for spin-down¹⁰, however, showed only qualitative agreement with Briley and Walls' results for $Re = 1167$. The observed differences are thought to be due to grid size effects.

The present computations have also been compared with LDV measurements taken by Watkins and Hussey⁹. Figure 7 presents comparisons of azimuthal velocity along the cylinder mid-plane at four instants during spin-up for a case with $a = 1.515$, $Re = 3076$. Figure 8 shows similar comparisons for

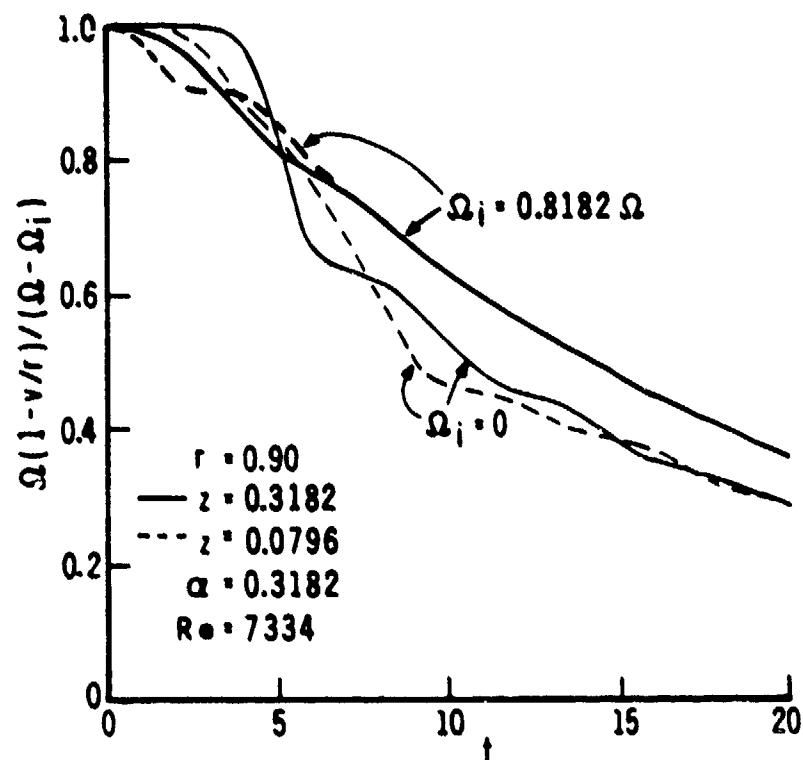


Figure 5. Comparison of inertial oscillations during spin-up from rest and from a previous state of rigid-body rotation.

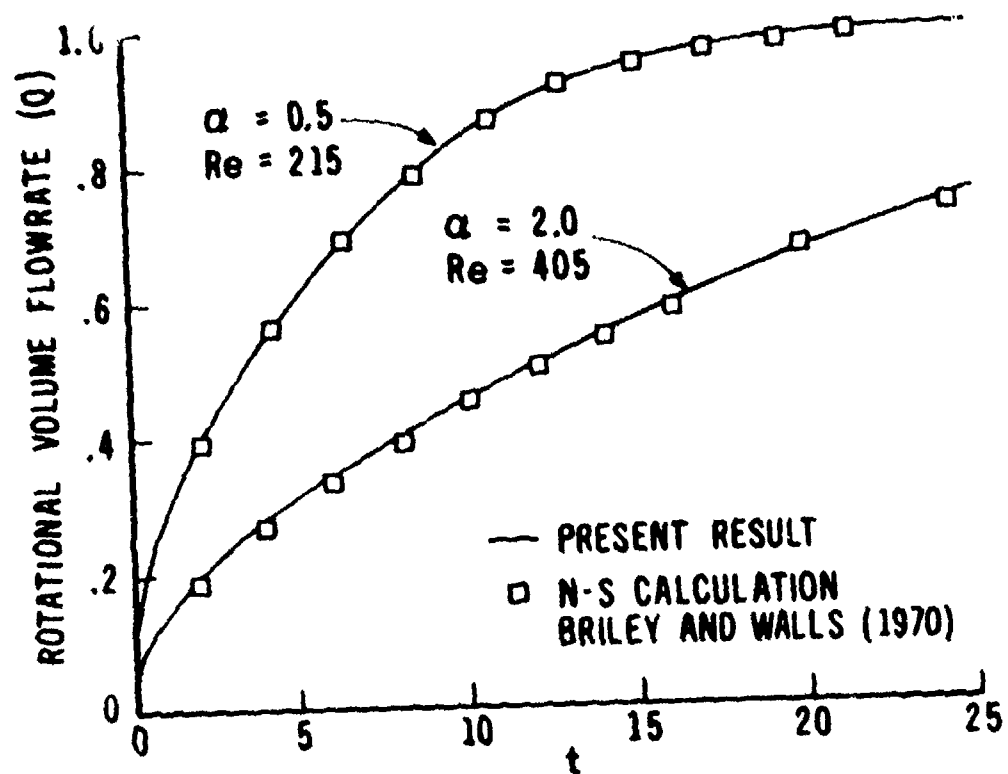


Figure 6. Rotational volume flow rate for spin-up from rest.

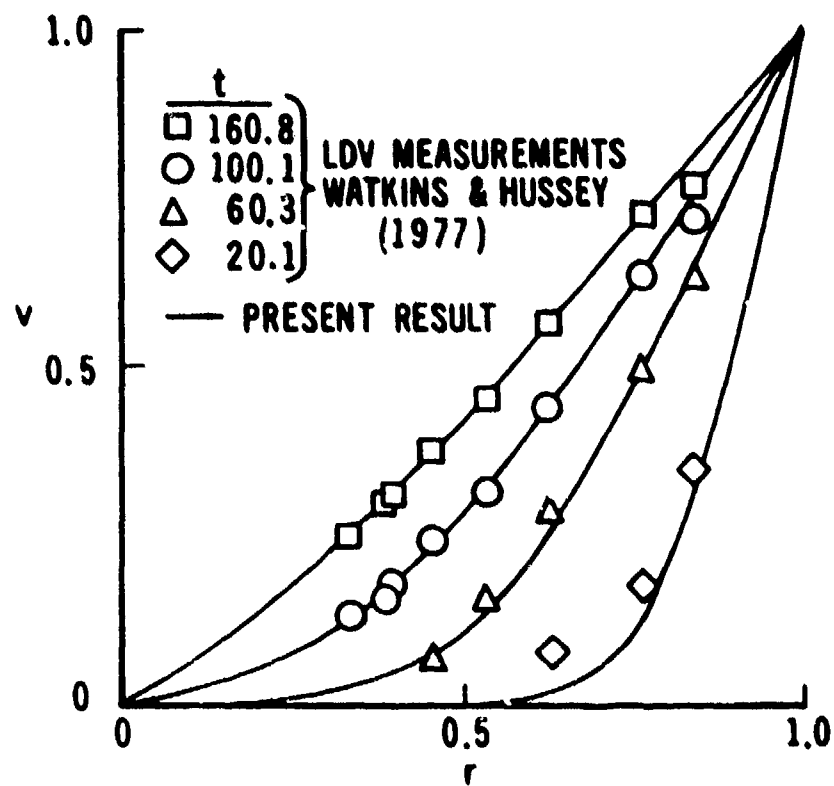


Figure 7. Azimuthal velocity profiles at cylinder mid-plane for $\alpha = 1.515$, $Re = 3076$.

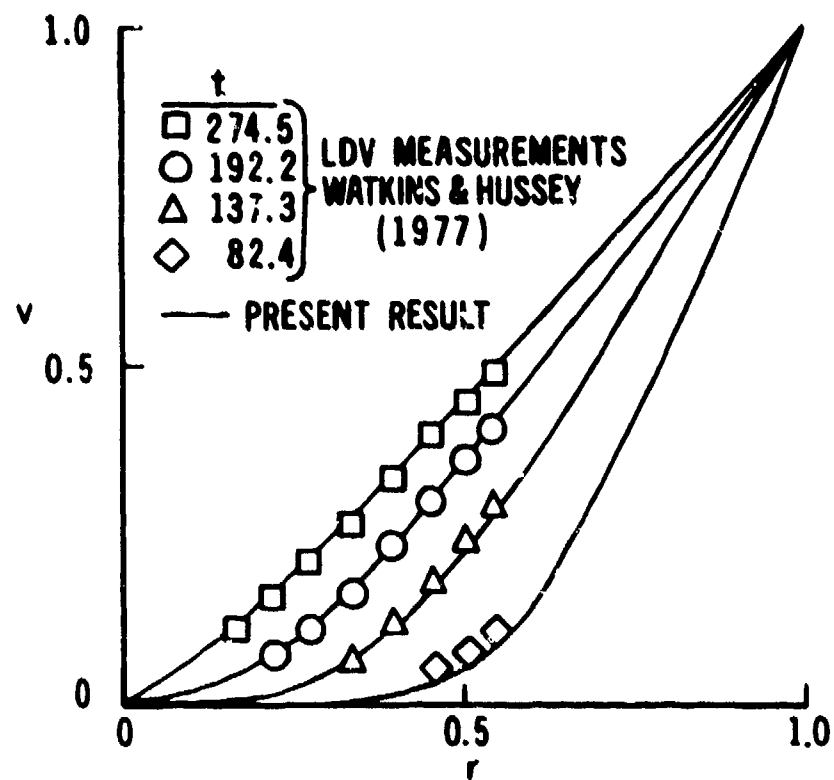


Figure 8. Azimuthal velocity profiles at cylinder mid-plane for $\alpha = 1$, $Re = 941.6$.

$a = 1$, $Re = 9741.6$. The size of the symbols used to plot the experimental data in Figures 7 and 8 approximately represents the size of the error bars that should be attached to these data. The calculations in Figure 8 used a 21×21 grid with $d = e = 0.10$ and required 2745 time steps with $\Delta t = 0.10$ to reach $t = 274.5$. Approximately 1-2 iterations were required per time step to satisfy Equations (18). It is interesting to note that the PCMI solution required only 69s of CPU time on the CDC 7600, whereas the experimental spin-up process depicted in Figure 8 required 150s.

The results shown in Figures 6, 7 and 8 are representative of the "core" flow in Wedemeyer's model of spin-up from rest and they can be predicted fairly well using that model; the accuracy of the prediction increases as Re increases. However, Wedemeyer's model says very little about the flow in the Ekman layers, in the corner region, and along the sidewall. These phenomena will be discussed next.

VI. TRANSIENT PHENOMENA AT EARLY TIME

The calculations were used to examine the details of the spin-up flow in the endwall Ekman layers and investigate transient reversed flow regions that develop and then decay along the sidewall during the first few rotations after the impulsive start. The latter phenomena are illustrated in Figures 9a-d. Instantaneous streamlines are shown for the Watkins and Hussey case with $a = 1$, $Re = 9741.6$, based on calculations performed with a 41×41 grid with $d = e = 0.1$ and $\Delta t = 0.05$. The calculations predict the development of several weak reversed flow regions in the meridional flow along the sidewall. A single reversed flow region has formed near the corner by $t = 6$ (see Figure 9b); two such regions have formed along the sidewall by $t = 13$ and there are four present by $t = 20$ (see Figure 9c). These weak reversed flow regions "collapse" in the next half-rotation or so (see Figure 9d for $t = 24$) and do not redevelop for $t > 24$. Grid convergence studies for this case show that the quantitative results in Figures 9 are sensitive to grid size; nevertheless, the qualitative presence of the reversed flow regions is predicted for calculations with 11×11 , 21×21 and 41×41 grids.

The transient reversed flow regions do not develop in calculations for $a = 1$, $Re \leq 1000$, possibly because of the large amount of viscous dissipation. At higher Re there is less viscous dissipation present and inertial effects become more pronounced. At very early time the inertial oscillations are confined to a thin layer of rotating fluid along the sidewall. Fluid particles near the endwall are accelerated radially outward in a spiral motion as the Ekman layer develops. These particles overshoot their "equilibrium radial position" before they turn upward from the edge of the Ekman layer near the corner. The reversed flow regions that develop along the sidewall are apparently linked to the inertial oscillations developed as swirling fluid particles travel upward along the sidewall and begin to migrate radially inward. As Re

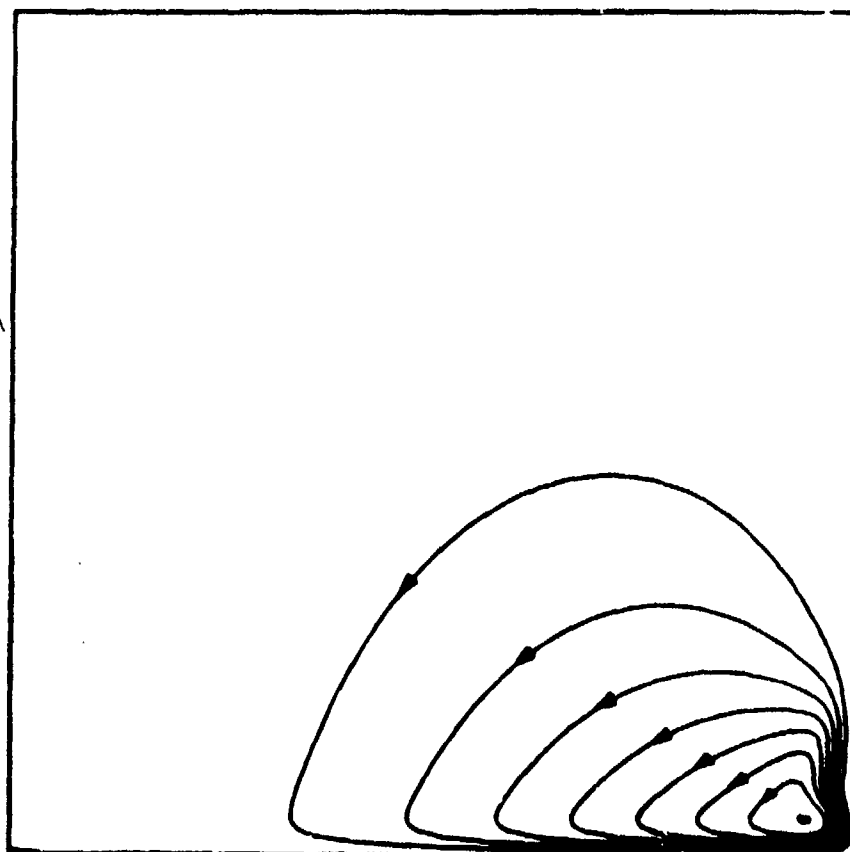


Figure 9a. Instantaneous streamlines in meridional plane for $\alpha = 1$, $Re = 9741.6$, $\Delta\psi = 0.0004$, $t = 3$; $\psi_{min} = 0$, $\psi_{max} = 0.00322$.

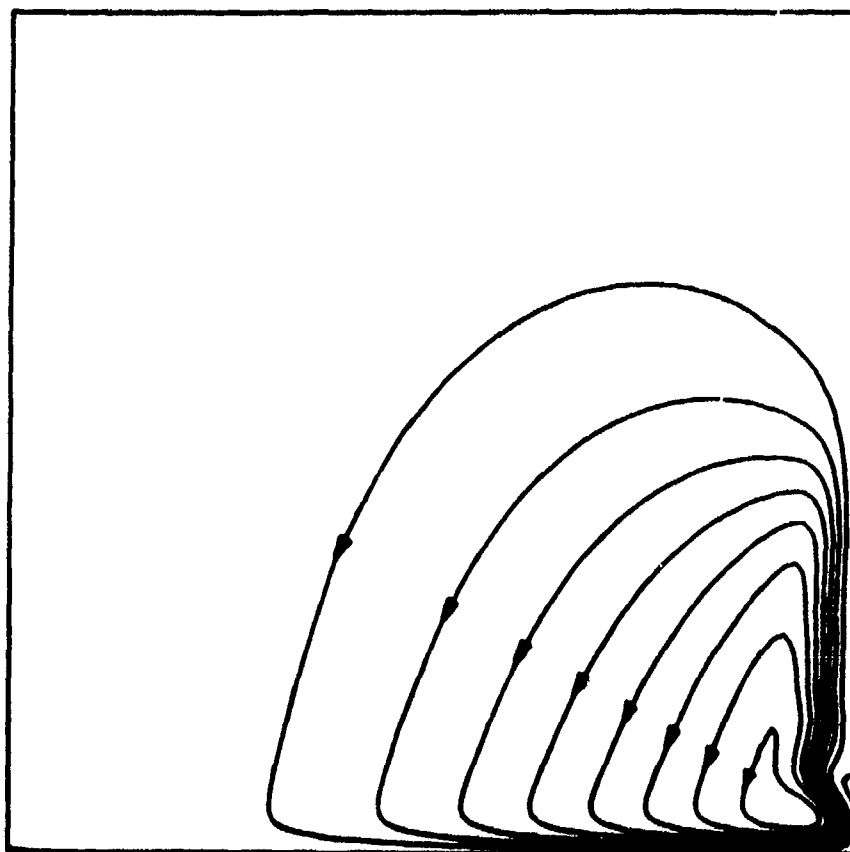


Figure 9b. Streamlines for $t = 6$; $\psi_{\min} = -0.00003$,
 $\psi_{\max} = 0.00350$. Closed contour along
sidewall indicates reversed flow region.

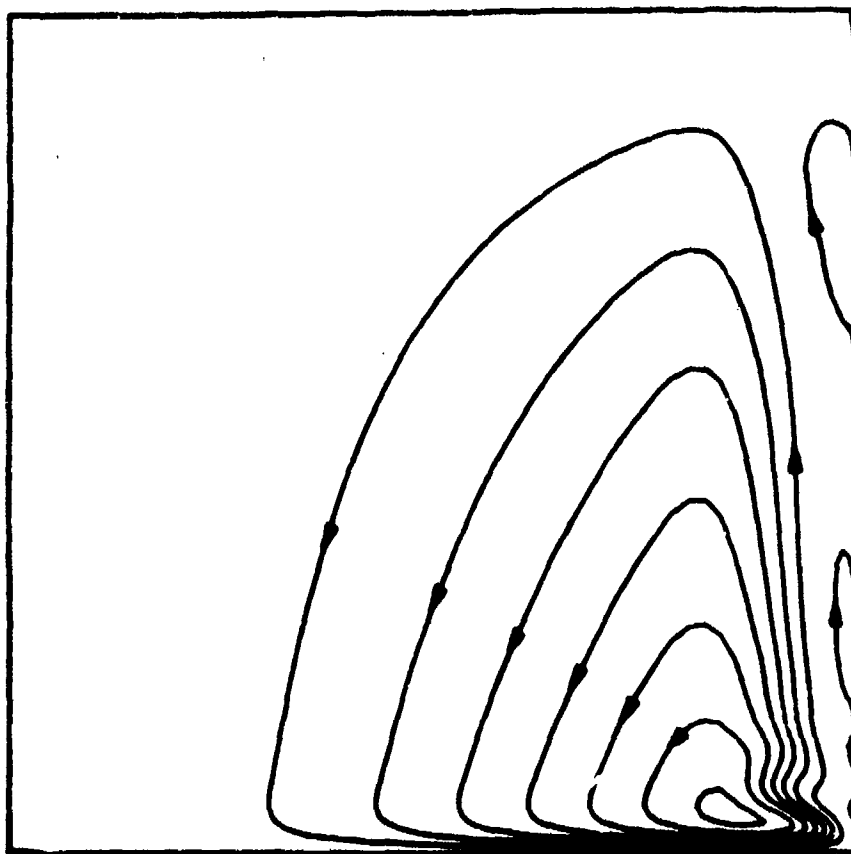


Figure 9c. Streamlines for $t = 20$; $\psi_{\min} = -0.00003$,
 $\psi_{\max} = 0.00294$.

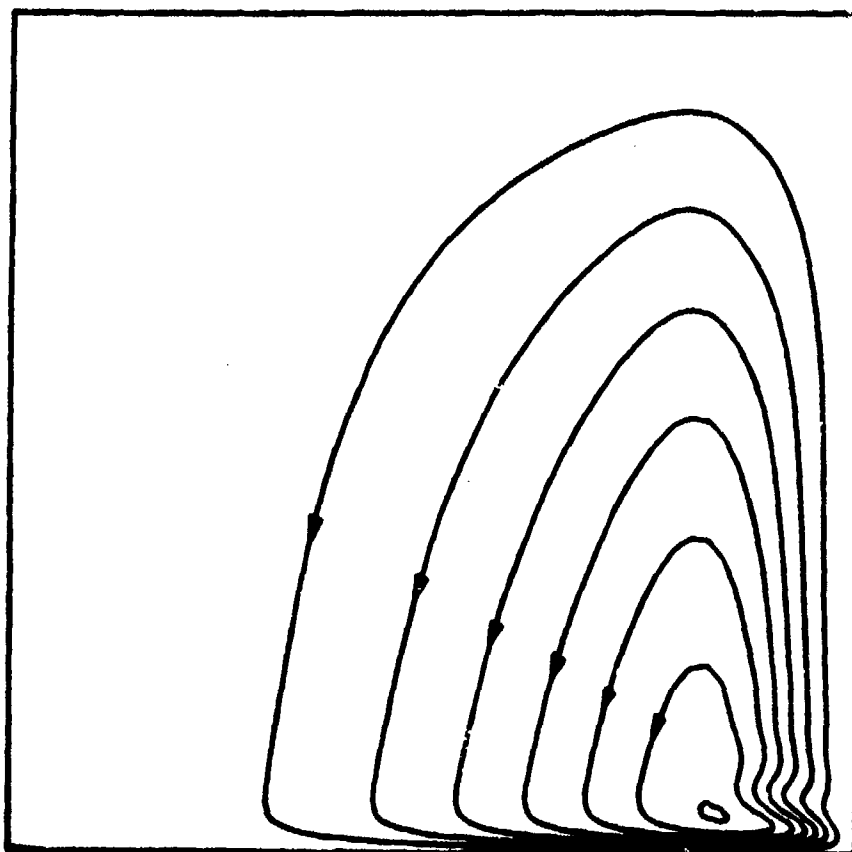


Figure 9d. Streamlines for $t = 24$; $\psi_{\min} = 0$,
 $\psi_{\max} = 0.00284$.

increases, the calculations predict that both the inertial oscillations and reversed flow regions become more pronounced. Figure 10 shows instantaneous streamlines for $\alpha = 1$, $Re = 50,000$ and $t = 15$ obtained with a 41×81 grid with $d = e = 0.05$ and $\Delta t = 0.0125$. At this Reynolds number, the local oscillations in the corner region are more severe than at $Re = 9741.6$. The reversed flow regions present in Figure 10 dissipate completely by $t = 50$. Grid convergence studies for this case indicate that the finite-difference resolution for this transformed 41×81 grid is inadequate to resolve the fine scales of the motion present in the corner region at early time; this case had 315 grid points in the corner region defined by $0.9 \leq r \leq 1$, $0 \leq z \leq 0.2$. Similar calculations for $\alpha = 1$, $Re = 1 \times 10^5$ developed a numerical instability at $t = 4.6$; the allowable value of Δt , given by Equation (19), approached zero due to the extreme severity of the local oscillations in the corner. This may indicate the development of a physical instability at this high Reynolds number.

It is possible that the reversed flow regions observed in these calculations are related to a physical phenomenon observed in Weidman's spin-up experiments¹⁶ for $Re = 5.9 \times 10^5$. He conducted experiments for $\alpha = 1.93$ using various wall acceleration rates and found that for wall accelerations $\geq 4 \text{ rad/s}^2$ a "turbulent column" formed along the sidewall at early time and then it eventually disappeared, ... "leaving an entirely laminar approach to solid body rotation." Although the largest Reynolds number used in our calculations is much lower than 5.9×10^5 , one can speculate that the local reversed flow regions present in the numerical calculations at moderate Reynolds number are manifestations of the observed transient "turbulent column" observed by Weidman. Additional flow visualization experiments are required to investigate this further.

VII. EKMAN LAYER MASS FLOW AND COMPATIBILITY CONDITION DURING SPIN-UP

An accurate description of the Ekman layer radial mass flow is needed to establish an appropriate "compatibility condition" for use in the Wedemeyer spin-up model¹. The Wedemeyer model has been used by many investigators^{1,2,9,16,17,18} to study spin-up from rest. In this model the flow is split into two parts: the Ekman layer flow and the remainder

¹⁶P. D. Weidman, "On the Spin-Up and Spin-Down of a Rotating Fluid, Part 2. Measurements and Stability," *J. Fluid Mech.*, Vol. 77, Pt. 4, 1976, pp. 709-735.

¹⁷P. D. Weidman, "On the Spin-Up and Spin-Down of a Rotating Fluid, Part 1. Extending the Wedemeyer Model," *J. Fluid Mech.*, Vol. 77, Pt. 4, 1976, pp. 685-708.

¹⁸H. Goller and H. Ranov, "Unsteady Rotating Flow in a Cylinder with a Free Surface," *J. Basic Eng.*, Trans. ASME, Vol. 90, Series D, December 1968, pp. 445-454.

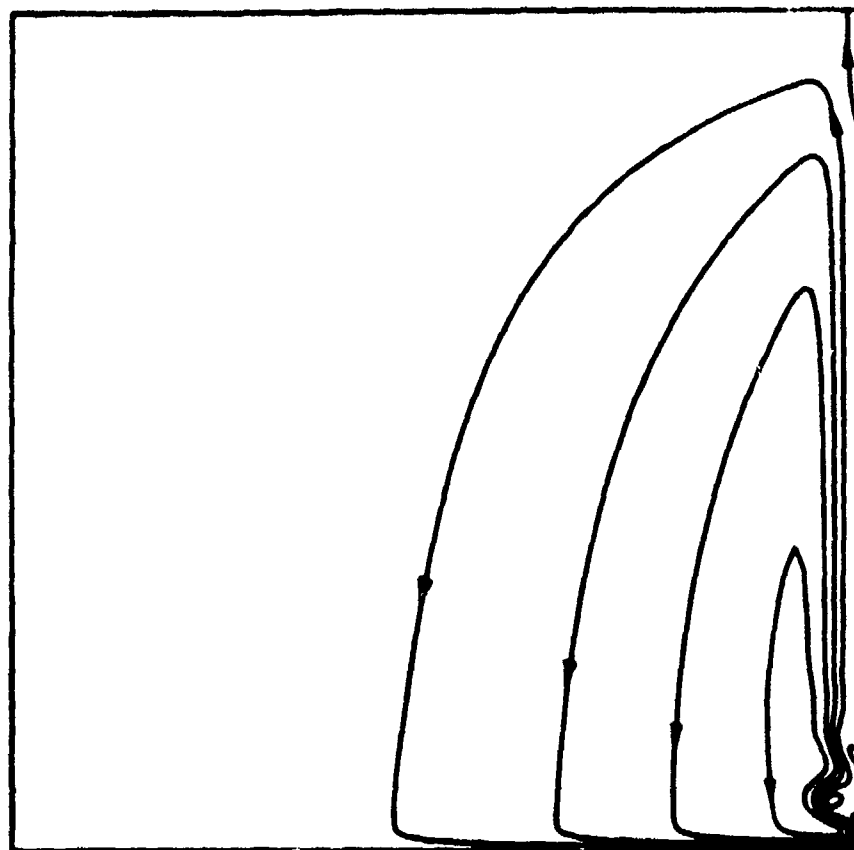


Figure 10. Instantaneous streamlines for $a = 1$,
 $Re = 50,000$, $t = 15$, with $\Delta\psi = 0.0004$;
 $\psi_{\min} = -0.00013$, $\psi_{\max} = 0.00177$.

of the flow, called the core flow. A partial differential equation for the core flow is derived from an order of magnitude analysis of the Navier-Stokes equations. In order to solve this equation, Wedemeyer postulates a compatibility condition, or functional relationship between the radial and azimuthal velocity components in the core, to approximate the coupling between the core flow and the flow in the Ekman layers. The radial mass flow rate in the Ekman layer, at a given radial position, prescribes the core radial velocity by conservation of mass. Wedemeyer developed his linear compatibility condition by interpolating between known results at $t = 0$ and ∞ ; it can be illustrated as shown in Figure 11. He assumed that this condition was valid as long as $Re < 3 \times 10^5$ and the Ekman layer remained laminar. Several investigators^{9,16,17,18} have used Rogers and Lance's numerical solutions¹⁹, for the laminar boundary-layer flow on an infinite rotating disk, in an attempt to construct a more accurate "non-linear" compatibility condition. These solutions, for various ratios of the outer flow-to-disk rotation rate, have been utilized to produce the non-monotonic compatibility condition shown in Figure 11. Weidman^{16,17} used the Rogers and Lance compatibility condition together with the Wedemeyer model and found that the non-monotonic behavior of the compatibility condition led to unrealistic double-valued solutions for azimuthal velocity. Since it is apparent from Weidman's results that the Rogers and Lance compatibility condition may be inappropriate for the spin-up problem, we have attempted to use the present numerical technique to quantify the Ekman layer mass flow rate during spin-up and investigate the degree of applicability of both the Wedemeyer and Rogers and Lance conditions.

In order to determine the instantaneous outward radial mass flow at a particular radial position along the endwall we had to adopt a definition for the "boundary-layer" edge in the Navier-Stokes calculations. We define this edge, δ , to be the last axial position away from the endwall where u passes through zero. The numerical results show u passes through zero only once in the interior at a particular radial position unless there is a temporary reversed flow region(s) present at that radial position. A typical radial velocity profile obtained from the Navier-Stokes solutions is shown in Figure 12 and compared with a corresponding Rogers and Lance boundary layer result for a non-rotating outer flow (the Von Karman problem); the core flow above the Ekman layer was not rotating for $t = 8.3$ and $r = 0.76$ in the present calculations. The two results in Figure 12 are almost identical as they should be according to the Wedemeyer model. The small differences are probably due to the fact that u does not asymptotically approach zero at the edge of the Ekman layer for spin-up in a finite cylinder. The Rogers and Lance calculations, on the other hand, impose this asymptotic behavior as a boundary condition.

¹⁹M. H. Rogers and G. N. Lance, "The Rotationally Symmetric Flow of a Viscous Fluid in the Presence of an Infinite Rotating Disk," J. Fluid Mech., Vol. 7, Pt. 4, April 1960, pp. 617-631.

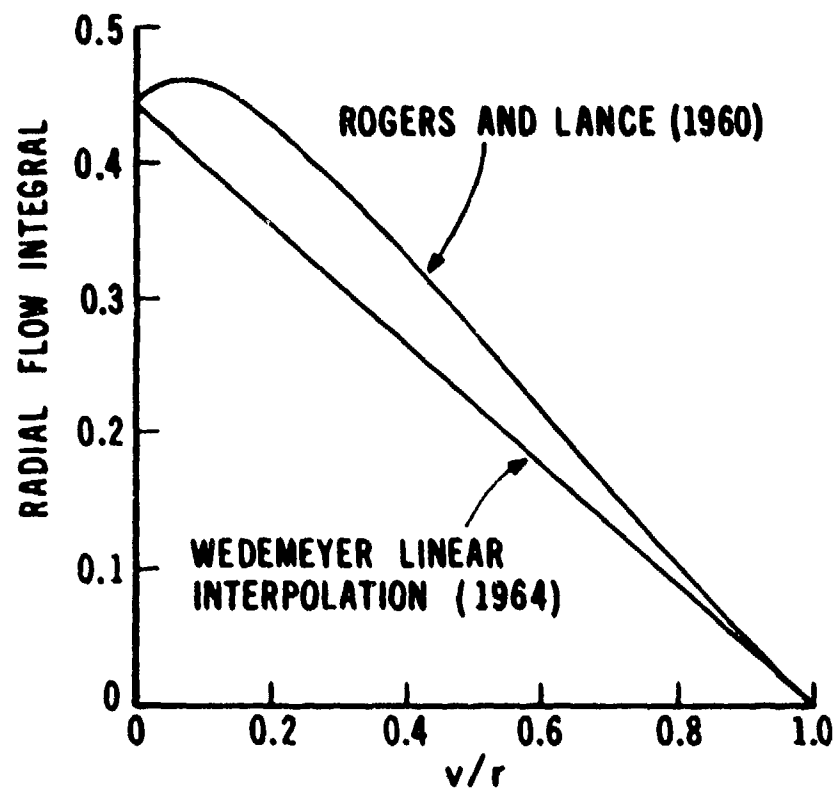


Figure 11. Ekman layer compatibility conditions.

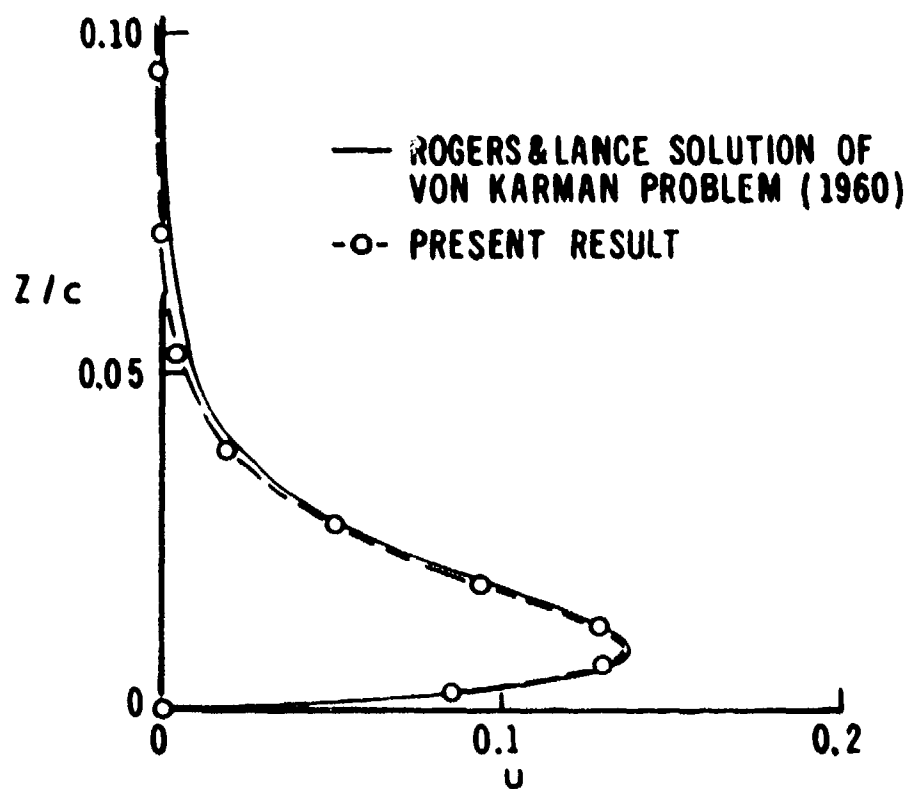


Figure 12. Radial velocity profiles in Ekman layer at $r = 0.76$ for $a = 1$, $Re = 9741.6$ and $t = 8.3$.

For purposes of the present comparison, the nondimensional Ekman layer radial mass flow rate, \dot{m} , is determined from the numerical results using the relation

$$\dot{m} = \psi_\delta \sqrt{Re}/r^2; \quad (21)$$

where ψ_δ represents the value of ψ at $z = \delta$, for a specified radial position. The value of v at $z = \delta$ is used to define the local value of v/r for comparison with the compatibility conditions in Figure 11. Both ψ_δ and v_δ are obtained from the numerical results by linear interpolation.

Figure 13 shows typical numerical results for \dot{m} as a function of v/r . Values for $\alpha = 2$, $Re = 9741.6$ are plotted for three radial positions and various values of t , indicated by the numbers adjacent to several points. According to these calculations the Ekman layer forms during approximately the first cylinder rotation, $t = 2\pi$; thereafter, it monotonically decays as t and v/r increase. The data in Figure 13 were obtained using results from 21×21 and 41×41 grids, together with Richardson quadratic extrapolation⁵, to approximate results for zero grid size. The validity of this approach was partially affirmed by approximating \dot{m} by the first two terms of ϵ series

$$\dot{m}_i = \dot{m}_0 + b (\Delta\eta_i)^l + \dots; \quad (22)$$

where \dot{m}_0 , b and l are unknown constants and \dot{m}_i represents the value of \dot{m} obtained with a particular grid size $\Delta\eta_i$. Numerical results for $\Delta\eta_i = 0.100, 0.050$ and 0.025 were used to determine the three constants in Equation (22) for representative r and t . The results show that $1.9 \leq l \leq 5.7$, indicating that the actual variation is no more extreme than that given by Richardson's result with $l = 2$. The results in Figure 13 are typical of those for calculations performed over the parameter range $1 \leq \alpha \leq 4.4$ and $405 \leq Re \leq 5 \times 10^4$. The complete set of numerical results, together with grid convergence studies performed for $\alpha = 1$, $Re = 1000, 9741.6$ and 5×10^4 , supports the following conclusions:

- a. the Ekman layer mass flow at a given radial position decreases monotonically as v/r and t increase for $t \geq 2\pi$;
- b. there is no unique compatibility condition that is valid in an exact sense for all α , Re , r and t ;
- c. a new compatibility condition can be constructed that gives a better approximation to the present numerical data than either the Rogers and Lance or the Wedemeyer compatibility condition.

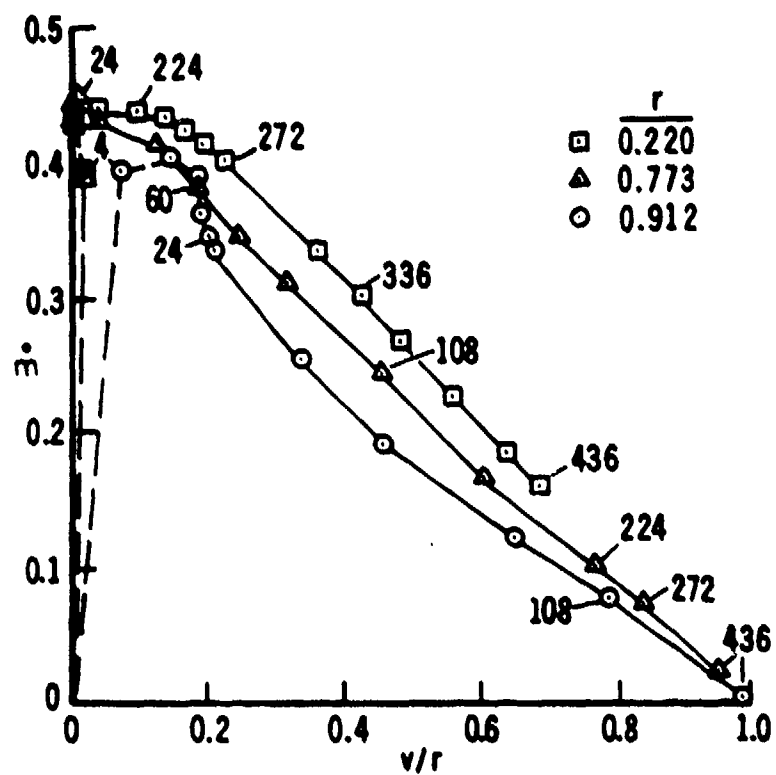


Figure 13. Ekman layer radial mass flow predicted for $\alpha = 2$, $Re = 9741.6$ using Richardson extrapolation.

The data for $1 \leq \alpha \leq 4.4$ and $405 \leq Re \leq 5 \times 10^4$ have been used to develop a new compatibility condition and to determine its error. It was constructed by expressing the average value of \dot{m} at $r = 0.5$ as a function of (v/r) . A simple monotonic function that approximates the numerical data is

$$\dot{m} = \begin{cases} (.443/9)[16 (v/r)^3 - 24 (v/r)^2 + 9] & \text{for } 0 \leq (v/r) \leq 0.75 \\ (.443) [1 - (v/r)] & \text{for } 0.75 \leq (v/r) \leq 1. \end{cases} \quad (23)$$

It is plotted in Figure 14 and compared with the Wedemeyer and Rogers and Lance conditions. In general, the calculated \dot{m} is larger than predicted by Equation (23) for $r < 0.5$ and smaller for $r > 0.5$; this trend is apparently due to a radial variation in \dot{m} caused by the presence of the sidewall. The curve described by Equation (23) falls between the Wedemeyer and Rogers and Lance curves for $0 < v/r < 0.75$ and is coincident with the Wedemeyer curve for $0.75 \leq v/r \leq 1$; it has a continuous first derivative over the interval $[0,1]$. The shaded band represents the maximum "scatter" present in the numerical data for $t > 2\pi$, $1 \leq \alpha \leq 4.4$, $405 \leq Re \leq 5 \times 10^4$. For $0 \leq t \leq 2\pi$ the mass flow is less than that indicated by the shaded band for a given (v/r) ; this early time behavior is not described by Equation (23) and is outside the scope of the Wedemeyer theory. Note that Equation (23) is not fitted to the center of the shaded band; rather, it is purposely fitted to the $r = 0.5$ data to weight the results toward the center of the endwall and attempt to make it equally valid for $r < .5$ and $r > .5$. A curve fitted to the center of the shaded band would weight the results toward the sidewall where the radial variation in \dot{m} is most pronounced. This would result in a relatively poor approximation to \dot{m} near the center of the cylinder. It should be noted that the adoption of the compatibility condition given by Equation (23) leads to errors in the nondimensional mass flow rate predicted at a given r and t (and hence the core radial velocity in the Wedemeyer model) of as much as approximately 20% of the maximum value, 0.443. This rather large error is inherent in any compatibility condition that neglects the radial variation of mass flow. We expect that the compatibility condition given by Equation (23) should be equally valid for $\alpha > 4.4$ and $Re > 5 \times 10^4$ as long as the Ekman layer remains laminar. A compatibility condition appropriate for a turbulent Ekman layer cannot be developed using results from the present numerical procedure.

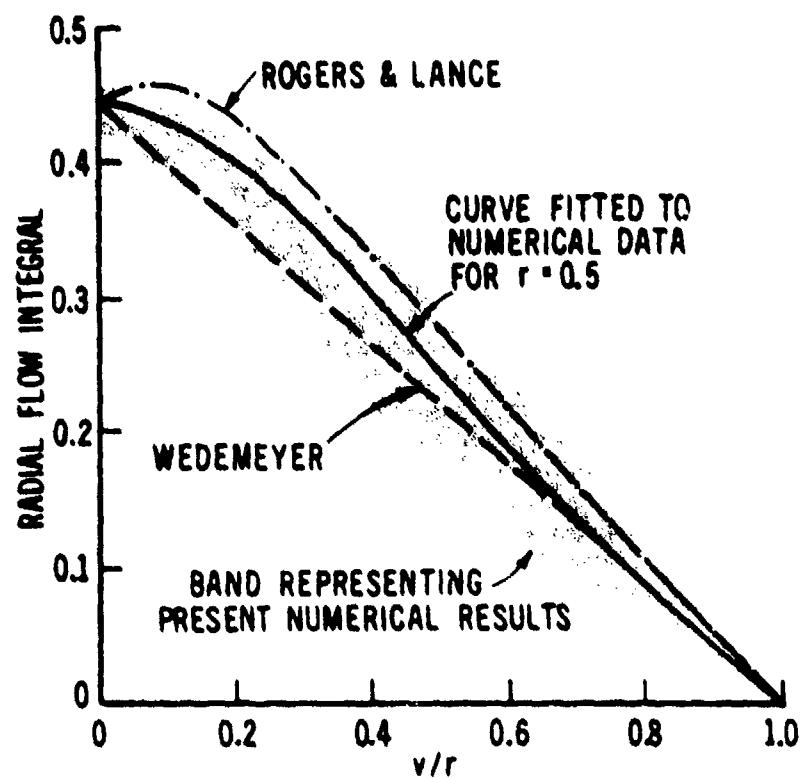


Figure 14. Comparison of compatibility conditions with band representing numerical data for $1 \leq \alpha \leq 4.4$ and $405 \leq Re \leq 50,000$.

VIII. CONCLUSIONS

A predictor-corrector multiple-iteration method has been combined with the Gauss-Seidel iteration technique to produce an accurate and efficient numerical procedure for solving the unsteady Navier-Stokes equations. Test calculations for spin-up in a cylinder were shown to be consistent with previous calculations and/or experimental measurements. Computations carried out for $0.5 \leq a \leq 4.4$ and $205 \leq Re \leq 50,000$ showed that coordinate transformations could be used to simultaneously resolve details of both the interior and boundary layer flows using a moderate number of grid points. These calculations demonstrated the presence of inertial oscillations and temporary reversed flow regions along the sidewall during spin-up from rest. Computational experiments have been performed to determine the radial mass flow in the endwall Ekman layers during spin-up and investigate the accuracy of compatibility conditions used in the Wedemeyer spin-up model. A new compatibility condition has been developed based on the results of this numerical study.

ACKNOWLEDGMENT

The author is grateful to Dr. R. Sedney and Mr. N. Gerber for their advice and encouragement concerning this work.

APPENDIX A

TRANSFORMED EQUATIONS AND BOUNDARY CONDITIONS

The Navier-Stokes equations, Equations (1) - (3), and boundary conditions, Equations (11), are transformed from the (r, z) physical plane to the (β, η) computational plane using the analytical transformations given by Equations (12). The transformed governing equations are

$$\begin{aligned} \gamma_r = & \gamma_\beta [Re^{-1} (\beta_{rr} - \beta_r/r) - \beta_r \eta_z \gamma_\eta / r] \\ & + \gamma_\eta [Re^{-1} \eta_{zz} + \beta_r \eta_z \gamma_\beta / r] \\ & + Re^{-1} [(\beta')^2 \gamma_{\beta\beta} + (\eta')^2 \gamma_{\eta\eta}], \end{aligned} \quad (A-1)$$

$$\begin{aligned} \zeta_r = & \zeta_\beta [Re^{-1} (\beta_{rr} + \beta_r/r) - \beta_r \eta_z \gamma_\eta / r] \\ & + \zeta_\eta [Re^{-1} \eta_{zz} + \beta_r \eta_z \gamma_\beta / r] \\ & + Re^{-1} [(\beta')^2 \zeta_{\beta\beta} + (\eta')^2 \zeta_{\eta\eta}] + 2 \gamma \gamma_\eta \eta_z / r^3 \\ & + \zeta [-Re^{-1} / r^2 + \eta_z \gamma_\eta / r^2], \end{aligned} \quad (A-2)$$

$$\begin{aligned} \gamma_{\beta\beta} + (\eta_z / \beta_r)^2 \gamma_{\eta\eta} = & r \zeta / (\beta_r)^2 - \eta_{zz} \gamma_\eta / (\beta_r)^2 \\ & + [1 / (r \beta_r) - \beta_{rr} / (\beta_r)^2] \gamma_\beta; \end{aligned} \quad (A-3)$$

where

$$\beta_r = 2\bar{b} / ((\bar{b} + r)(\bar{b} - r) \ln [(\bar{b} + 1)/(\bar{b} - 1)]), \quad (A-4)$$

$$\beta_{rr} = 2r\beta_r / [(\bar{b} + r)(\bar{b} - r)], \quad (A-5)$$

$$\eta_z = 2\bar{c} / (a(\bar{c} + z/a - 1)(\bar{c} - z/a + 1) \ln [(\bar{c} + 1)/(\bar{c} - 1)]), \quad (A-6)$$

$$\eta_{zz} = 2(z/a - 1) \eta_z / [a(\bar{c} + z/a - 1)(\bar{c} - z/a + 1)], \quad (A-7)$$

with $b = (1 - d)^{-1/2}$ and $c = (1 - e)^{-1/2}$.

The transformed boundary conditions become

$$\psi(t, 0, \eta) = \gamma(t, 0, \eta) = \zeta(t, 0, \eta) = 0, \quad (\text{A-8})$$

$$\psi(t, 1, \eta) = 0, \quad \gamma(t, 1, \eta) = 1, \quad (\text{A-9})$$

$$\psi(t, \beta, 0) = 0, \quad \gamma(t, \beta, 0) = r^2, \quad (\text{A-10})$$

$$\psi(t, \beta, 1) = \zeta(t, \beta, 1) = \gamma_{\eta}(t, \beta, 1) = 0, \quad (\text{A-11})$$

$$\zeta(t, 1, \eta) = (\beta_r)^2 \psi_{\beta\beta}, \quad (\text{A-12})$$

$$\zeta(t, \beta, 0) = (\eta_z)^2 \psi_{\eta\eta}/r, \quad (\text{A-13})$$

where

$$r = \bar{b}([(\bar{b} + 1)/(\bar{b} - 1)]^B - 1)/([(\bar{b} + 1)/(\bar{b} - 1)]^B + 1), \quad (\text{A-14})$$

APPENDIX B

FINITE-DIFFERENCE EQUATIONS

The finite-difference approximations given by Equations (13) form the basis of the finite-difference equations representing Equations (A-1) and (A-2). Uncoupled linear difference equations are constructed with the PCMI method by approximating γ_B and γ_n in Equations (A-1) and (A-2) and γ and γ_n in Equation (A-2) as known constants, specified from either the extrapolated value or the value calculated at the previous iteration level. The coupling between equations and the nonlinearities of individual terms are approximated by the multiple-iteration process which updates γ_B , γ_n , γ and γ_n at each subsequent iteration level. In the present difference procedure, station $(i+1, j, k)$ in Figure 3 is calculated from known information at stations $(i+1, j, k-1)$, $(i+1, j, k+1)$, (i, j, k) and $(i-1, j, k)$. Stations $(i+1, j-1, k)$ and $(i+1, j+1, k)$ are treated as unknowns, resulting in a tridiagonal system of equations for Equations (A-1) and (A-2). The γ -difference equation is given by the tridiagonal system

$$a_{1j} \gamma_{i+1, j-1, k}^{m+1} + b_{1j} \gamma_{i+1, j, k}^{m+1} + c_{1j} \gamma_{i+1, j+1, k}^{m+1} = d_{1j} ; \quad (B-1)$$

where

$$a_{1j} = \{(\beta_{rr} - \beta_r/r)/Re - \eta_z \beta_r \gamma_n/r\}/(2\Delta\beta) - (\beta_r/\Delta\beta)^2/Re, \quad (B-2)$$

$$b_{1j} = 3/(2\Delta t) + 2 [(\beta_r/\Delta\beta)^2 + (\eta_z/\Delta\eta)^2]/Re, \quad (B-3)$$

$$c_{1j} = -a_{1j} - 2(\beta_r/\Delta\beta)^2/Re, \quad (B-4)$$

$$\begin{aligned} d_{1j} = & (4 \gamma_{i, j, k} - \gamma_{i-1, j, k})/(2\Delta t) \\ & + (\gamma_{i+1, j, k+1}^{(m)} - \gamma_{i+1, j, k-1}^{(m)}) (\eta_{zz}/Re + \eta_z \beta_r \gamma_B/r)/(2\Delta\eta) \\ & + (\gamma_{i+1, j, k+1}^{(m)} + \gamma_{i+1, j, k-1}^{(m)}) (\eta_z/\Delta\eta)^2/Re. \end{aligned} \quad (B-5)$$

The ζ -difference equation is given by the tridiagonal system

$$a_{2j} \zeta_{i+1,j-1,k}^{(m+1)} + b_{2j} \zeta_{i+1,j,k}^{(m+1)} + c_{2j} \zeta_{i+1,j+1,k}^{(m+1)} = d_{2j} ; \quad (B-6)$$

where

$$a_{2j} = a_{1j} + \beta_r / (r \Delta \theta \text{ Re}), \quad (B-7)$$

$$b_{2j} = b_{1j} + (1/\text{Re} - \eta_z \psi_n) / r^2, \quad (B-8)$$

$$c_{2j} = c_{1j} - 2 \beta_r / (r \text{ Re}), \quad (B-9)$$

$$\begin{aligned} d_{2j} = & (4 \zeta_{i,j,k} - \zeta_{i-1,j,k}) / (2\Delta t) \\ & + (\zeta_{i+1,j,k+1}^{(m)} - \zeta_{i+1,j,k-1}^{(m)}) (\eta_{zz} / \text{Re} + \eta_z \rho_r \psi_g / r) / (2\Delta n) \\ & + (\zeta_{i+1,j,k+1}^{(m)} + \zeta_{i+1,j,k-1}^{(m)}) (\eta_z / \Delta n)^2 / \text{Re} \\ & + (\psi_{i+1,j,k}^{(m)} (\psi_{i+1,j,k+1}^{(m)} - \psi_{i+1,j,k-1}^{(m)}) (\eta_z / \Delta n) / r^3. \end{aligned} \quad (B-10)$$

The finite-difference approximations given by Equations (14) form the basis of the finite-difference equations representing Equation (A-3). The quantity ζ in Equation (A-3) is specified from either the extrapolated value or the value calculated at the most recent t -iteration level. In the Gauss-Seidel procedure used to solve Equation (A-3), station $(i+1,j,k)$ is calculated from known information at stations $(i+1,j-1,k)$, $(i+1,j+1,k)$, $(i+1,j,k-1)$ and $(i+1,j,k+1)$. The ψ -difference equation is given by

$$\begin{aligned} \psi_{i+1,j,k}^{(m+1)} = & \left\{ (\psi_{i+1,j+1,k}^{(m)} + \psi_{i+1,j-1,k}^{(m+1)}) (\beta_r / \Delta \theta)^2 \right. \\ & + (\psi_{i+1,j,k+1}^{(m)} + \psi_{i+1,j,k-1}^{(m+1)}) (\eta_z / \Delta n)^2 \\ & + (\psi_{i+1,j+1,k}^{(m)} - \psi_{i+1,j-1,k}^{(m+1)}) (\beta_{rr} - \beta_r / r) / (2 \Delta \theta) \end{aligned} \quad (\text{Cont'd})$$

(cont'd)

$$+ (\psi_{i+1,j,k+1}^{(m)} - \psi_{i+1,j,k-1}^{(m+1)}) (\eta_{zz}) / (2 \Delta \eta) \\ - r \psi_{i+1,j,k}^{(n)} \Bigg\} / [2(R_r/\Delta B)^2 + 2(\eta_z/\Delta \eta)^2] ; \quad (B-11)$$

where $\psi_{i+1,j-1,k}^{(m+1)}$ and $\psi_{i+1,j,k-1}^{(m+1)}$ are both known quantities due to the order in which the calculations are performed.

The difference equations shown in this Appendix are solved using the numerical procedure described in Section III.

LIST OF SYMBOLS

a	cylinder radius
b, c, m_0	constants in Equation (22)
b, \bar{c}, d, e	coordinate transformation constants
c	cylinder half-height
Ek	Ekman number [$= \nu / (\Omega c^2)$]
i	time subscript
j	radial subscript
k	axial subscript
m	t -iteration superscript
\dot{m}	nondimensional Ekman layer radial mass flow rate
n	γ -iteration superscript
r, R	nondimensional and dimensional radial coordinate
Re	Reynolds number [$= \Omega a^2 / \nu$]
t, T	nondimensional and dimensional time
u, v, w	r, θ, z nondimensional velocity components
z, Z	nondimensional and dimensional axial coordinate
α	cylinder aspect ratio [$= c/a$]
β	transformed radial coordinate
γ, Γ	nondimensional and dimensional circulation
δ	Ekman layer edge
ϵ	iteration convergence criteria
ζ, Z	nondimensional and dimensional vorticity
η	transformed axial coordinate
θ	azimuthal coordinate
ν	liquid kinematic viscosity
Ψ, ψ	nondimensional and dimensional stream function
Ω	final cylinder rotation rate
Ω_i	initial cylinder rotation rate
$\Delta B, \Delta n$	grid sizes in β and η coordinates

DISTRIBUTION LIST

<u>No. of Copies</u>	<u>Organization</u>	<u>No. of Copies</u>	<u>Organization</u>
12	Commander Defense Documentation Center ATTN: DDC-DDA Cameron Station Alexandria, VA 22314	1	Commander US Army Communications Rsch and Development Command ATTN: DRICD-PPA-SA Fort Monmouth, NJ 07703
1	Commander US Army Waterways Experiment Station ATTN: R.H. Malter Vicksburg, MS 39180	1	Commander US Army Electronics R&D Command Technical Support Activity ATTN: DELSD-L Fort Monmouth, NJ 07703
1	Commander US Army Materiel Development and Readiness Command ATTN: DRCDMD-ST 5001 Eisenhower Avenue Alexandria, VA 22333	3	Commander US Army Missile Research and Development Command ATTN: DRDMI-R DRDMI-YDL DRDMI-TB, Mr. R. Deep Redstone Arsenal, AL 35809
3	Commander US Army Armament Research and Development Command ATTN: DRDAR-LCA-F, A. Loeb DRDAR-TSS (2cys) Dover, NJ 07801	1	Commander US Army Tank Automotive Research and Development Command ATTN: DRDTA-UL Warren, MI 48090
1	Commander US Army Armament Materiel Readiness Command ATTN: DRSAR-LEP-L, Tech Lib Rock Island, IL 61299	1	Commander US Army Jefferson Proving Ground ATTN: STEJP-TD-D Madison, IN 47250
1	Commander US Army Aviation Research and Development Command ATTN: DRSAR-E 12th and Spruce Streets St. Louis, MO 63166	1	Commander US Army Research Office ATTN: Dr. R.E. Singleton P.O. Box 12211 Research Triangle Park North Carolina 27709
2	Commander US Army Air Mobility Research and Development Laboratory ATTN: SAVDL-D, W.J. McCroskey Ames Research Center Moffett Field, CA 94035	1	Director US Army TRADOC Systems Analysis Activity ATTN: ATAA-SL, Tech Lib White Sands Missile Range, NM 88002

DISTRIBUTION LIST

<u>No. of Copies</u>	<u>Organization</u>	<u>No. of Copies</u>	<u>Organization</u>
5	Commander Naval Air Systems Command ATTN: AIR-604 Washington, DC 20360	2	Sandia Laboratories ATTN: F.G. Blottner Tech Lib Albuquerque, NM 87115
3	Commander Naval Ordnance Systems Cmd ATTN: ORD-0632 ORD-035 ORD-5524 Washington, DC 20360	6	Director National Aeronautics and Space Administration ATTN: D.R. Chapman J. Marvin J.D. Murphy R. MacCormack W.C. Rose H. Lomax Ames Research Center Moffett Field, CA 94035
2	Commander David W. Taylor Naval Ship Research & Development Cmd ATTN: H.J. Lugt, Code 1802 S. de los Santos Head, High Speed Aerospace Division Bethesda, MD 20084	2	Director Jet Propulsion Laboratory ATTN: J.M. Mark Tech Lib 4800 Oak Grove Drive Pasadena, CA 91103
1	Commander Naval Surface Weapons Center ATTN: DX-21, Lib Br Dahlgren, VA 22448	4	Director National Aeronautics and Space Administration ATTN: E. Price J. South J.R. Sterrett Tech Library Langley Research Center Langley Station Hampton, VA 23365
6	Commander Naval Surface Weapons Center Applied Aerodynamics Division ATTN: K.R. Enkenhus M. Ciment K. Lobb S.M. Hastings A.E. Winkleman W.C. Ragsdale Silver Spring, MD 20910	1	Director National Aeronautics and Space Administration Lewis Research Center ATTN: MS 60-3, Tech Lib 21000 Brookpark Road Cleveland, OH 44135
1	AFATL (DLDL, Dr. D.C. Daniel) Eglin AFB, FL 32542		
2	AFI (W.L. Hankey; J.S. Shang) Wright-Patterson AFB, OH 45433		

DISTRIBUTION LIST

<u>No. of Copies</u>	<u>Organization</u>	<u>No. of Copies</u>
2	Director National Aeronautics and Space Administration Marshall Space Flight Center ATTN: A.R. Felix, Chief SGE-AERO-AE Dr. W.W. Fowles Huntsville, AL 35812	1 Center for Interdisciplinary Programs ATTN: Victor Zakay W. 177th Street & Harlem River Bronx, NY 10453
3	Aerospace Corporation ATTN: T.D. Taylor H. Mirels R.L. Varwig Aerophysics Lab P.O. Box 92957 Los Angeles, CA 90009	1 General Dynamics ATTN: Research Lib 2246 P.O. Box 748 Fort Worth, TX 76101
3	ARO, Inc. ATTN: J.D. Whitfield R.K. Matthews J.C. Adams Arnold AFB, TN 37389	1 General Electric Company ATTN: H.T. Nagamatsu Research and Development Laboratory (Comb. Bldg.) Schenectady, NY 12301
1	AVCO Systems Division ATTN: B. Reeves 201 Lowell Street Wilmington, MA 01887	1 General Electric Co., RESD ATTN: R.A. Larmour 3198 Chestnut Street Philadelphia, PA 19101
3	The Boeing Company Commercial Airplane Group ATTN: W.A. Bissell, Jr. MS 1W-82, Org 6-8340 P.E. Rubbert J.D. McLean Seattle, WA 98124	3 Grumman Aerospace Corporation ATTN: R.E. Melnik L.G. Kaufman B. Grossman, Rsch Dept Bethpage, NY 11714
2	Calspan Corporation ATTN: A. Ritter M.S. Holden P.O. Box 235 Buffalo, NY 14221	2 Lockheed-Georgia Company ATTN: B.H. Little, Jr. G.A. Pounds Dept. 72074, Zone 403 86 South Cobb Drive Marietta, GA 30062
		1 Lockheed Missile and Space Co. ATTN: Tech Info Center 3251 Hanover Street Palo Alto, CA 94304

DISTRIBUTION LIST

<u>No. of Copies</u>	<u>Organization</u>	<u>No. of Copies</u>	<u>Organization</u>
4	Martin-Marietta Laboratories ATTN: S.H. Maslen S.C. Traugott K.C. Wang H. Obrenski 1450 S. Rolling Road Baltimore, MD 21227	3	California Institute of Technology ATTN: Tech Lib H.B. Keller Mathematics Dept D. Cole Aeronautics Dept Pasadena, CA 91109
2	McDonnell Douglas Astronautics Corporation ATTN: J. Xerikow H. Tang 5301 Bolsa Avenue Huntington Beach, CA 92647	1	Cornell University Graduate School of Aero Engr ATTN: Library Ithaca, NY 14850
1	McDonnell-Douglas Corporation Douglas Aircraft Company ATTN: T. Cebeci 3855 Lakewood Boulevard Long Beach, CA 90801	2	Illinois Institute of Technology ATTN: M.V. Morkovin H.M. Nagib 3300 South Federal Chicago, IL 60616
1	Northrup Corporation Aircraft Division ATTN: S. Powers 3901 W. Broadway Hawthorne, CA 90250	1	The Johns Hopkins University ATTN: S. Corrsin Dept. of Mechanics and Materials Science Baltimore, MD 21218
1	United Aircraft Corporation Research Laboratories ATTN: M.J. Werle East Hartford, CT 06108	3	Massachusetts Institute of Technology ATTN: E. Covert H. Greenspan Tech Library 77 Massachusetts Avenue Cambridge, MA 02139
1	Vought Systems Division LTV Aerospace Corporation ATTN: J.M. Cooksey Ch. Gas Dynamics Lab, 2-53700 P.O. Box 5907 Dallas, TX 75222	2	North Carolina State University Mechanical and Aerospace Engineering Department ATTN: F.F. DeJarnette J.C. Williams Raleigh, NC 27607

DISTRIBUTION LIST

<u>No. of Copies</u>	<u>Organization</u>	<u>No. of Copies</u>	<u>Organization</u>
1	Northwestern University ATTN: S.H. Davis Dept of Eng Sci and Appl Math Evanston, IL 60201	1	Rensselaer Polytechnic Institute Department of Math Sciences ATTN: R.C. DiPrima Troy, NY 12181
1	Notre Dame University ATTN: T.J. Mueller Dept of Aero Engr South Bend, IN 46556	1	Rutgers University Department of Mechanical, Industrial and Aerospace Engineering ATTN: R.H. Page New Brunswick, NJ 08903
2	Ohio State University Dept of Aeronautical and Astronautical Engineering ATTN: S.L. Pertie O.R. Burggraf Columbus, OH 43210	1	Southern Methodist University Department of Civil and Mechanical Engineering ATTN: R.L. Simpson Dallas, TX 75275
2	Polytechnic Institute of New York ATTN: G. Moretti S.G. Rubin Route 110 Farmingdale, NY 11735	1	Southwest Research Institute Applied Mechanics Reviews 8500 Culebra Road San Antonio, TX 78228
4	Princeton University James Forrestal Research Center Gas Dynamics Laboratory ATTN: J.E. Vas S.M. Bogdonoff S.I. Cheng Tech Lib Princeton, NJ 08540	1	University of California- Berkeley Department of Aerospace Engineering ATTN: M. Holt Berkeley, CA 94720
1	Purdue University Thermal Science and Prop Center ATTN: D.E. Abbott W. Lafayette, IN 47907	1	University of California- Davis ATTN: H.A. Dwyer Davis, CA 95616
		2	University of California- San Diego Department of Aerospace Engineering and Mechanical Engineering Sciences ATTN: P. Libby Tech Library La Jolla, CA 92037

DISTRIBUTION LIST

<u>No. of Copies</u>	<u>Organization</u>	<u>No. of Copies</u>	<u>Organization</u>
1	University of Cincinnati Department of Aerospace Engineering ATTN: R.T. Davis Cincinnati, OH 45221	1	University of Texas Department of Aerospace Engineering ATTN: J.C. Westkaemper Austin, TX 78712
1	University of Colorado Department of Astro-Geophysics ATTN: E.R. Benton Boulder, CO 80302	1	University of Virginia Department of Aerospace Engineering and Engineering Physics ATTN: I.D. Jacobson Charlottesville, VA 22904
1	University of Hawaii Department of Ocean Engr ATTN: G. Venezian Honolulu, HI 96822	1	University of Washington Department of Mechanical Engineering ATTN: Tech Lib Seattle, WA 98195
2	University of Maryland ATTN: W. Melnik J.D. Anderson College Park, MD 20740	1	University of Wyoming ATTN: D.L. Boyer University Station Laramie, WY 82071
1	University of Michigan Department of Aeronautical Engineering ATTN: Tech Lib East Engineering Building Ann Arbor, MI 48104	2	Virginia Polytechnic Institute Department of Aerospace Engineering ATTN: G.R. Inger F.J. Pierce Blacksburg, VA 24061
1	University of Santa Clara Department of Physics ATTN: R. Greeley Santa Clara, CA 95053	1	Woods Hole Oceanographic Institute ATTN: J.A. Whitehead Woods Hole, MA 02543
3	University of Southern California Department of Aerospace Engineering ATTN: T. Maxworthy P. Weidman L.G. Redekopp Los Angeles, CA 90007		

DISTRIBUTION LIST

Aberdeen Proving Ground

Dir, USAMSAA

ATTN: Dr. J. Sperrazza
DRXSY-MP, H. Cohen

Cdr, USATECOM

ATTN: DRSTE-TO-F

Dir, Wpns Sys Concepts Team,

Bldg. E3516, EA

ATTN: DRDAR-ACW (M.C. Miller)

Cdr/Dir, USA CSL, EA

ATTN: Munitions Sys Div

Bldg. 3330

E.A. Jeffers

W.C. Dee

W.J. Pribyl

USER EVALUATION OF REPORT

Please take a few minutes to answer the questions below; tear out this sheet and return it to Director, US Army Ballistic Research Laboratory, ARRADCOM, ATTN: DRDAR-TSB, Aberdeen Proving Ground, Maryland 21005. Your comments will provide us with information for improving future reports.

1. BRL Report Number _____

2. Does this report satisfy a need? (Comment on purpose, related project, or other area of interest for which report will be used.)

3. How, specifically, is the report being used? (Information source, design data or procedure, management procedure, source of ideas, etc.)

4. Has the information in this report led to any quantitative savings as far as man-hours/contract dollars saved, operating costs avoided, efficiencies achieved, etc.? If so, please elaborate.

5. General Comments (Indicate what you think should be changed to make this report and future reports of this type more responsive to your needs, more usable, improve readability, etc.)

6. If you would like to be contacted by the personnel who prepared this report to raise specific questions or discuss the topic, please fill in the following information.

Name: _____

Telephone Number: _____

Organization Address: _____

